Editors' Suggestion Featured in Physics

Quantum Simulation of the Bosonic Creutz Ladder with a Parametric Cavity

Jimmy S. C. Hung,[1] J. H. Busnaina,[1] C. W. Sandbo Chang,[1] A. M. Vadiraj,[1]
I. Nsanzineza,[1] E. Solano,[2,3,4,5] H. Alaeian,[6] E. Rico,[4,5] and C. M. Wilson[1,*]
[1]*Institute for Quantum Computing and Department of Electrical and Computer Engineering, University of Waterloo, Waterloo, Ontario N2L 3G1, Canada*
[2]*Kipu Quantum, Kurwenalstrasse 1, 80804 Munich, Germany*
[3]*International Center of Quantum Artificial Intelligence for Science and Technology (QuArtist) and Department of Physics, Shanghai University, 200444 Shanghai, China*
[4]*Department of Physical Chemistry, University of the Basque Country UPV/EHU, Apartado 644, 48080 Bilbao, Spain*
[5]*IKERBASQUE, Basque Foundation for Science, Plaza Euskadi 5, 48009 Bilbao, Spain*
[6]*School of Electrical and Computer Engineering, Department of Physics and Astronomy, Quantum Science and Engineering Institute, Purdue University, West Lafayette, Indiana 47907, USA*

(Received 8 January 2021; accepted 22 July 2021; published 2 September 2021)

There has been a growing interest in realizing quantum simulators for physical systems where perturbative methods are ineffective. The scalability and flexibility of circuit quantum electrodynamics make it a promising platform for implementing various types of simulators, including lattice models of strongly coupled field theories. Here, we use a multimode superconducting parametric cavity as a hardware-efficient analog quantum simulator, realizing a lattice in synthetic dimensions with complex hopping interactions. The coupling graph, i.e., the realized model, can be programmed *in situ*. The complex-valued hopping interaction further allows us to simulate, for instance, gauge potentials and topological models. As a demonstration, we simulate a plaquette of the bosonic Creutz ladder. We characterize the lattice with scattering measurements, reconstructing the experimental Hamiltonian and observing important precursors of topological features including nonreciprocal transport and Aharonov-Bohm caging. This platform can be easily extended to larger lattices and different models involving other interactions.

DOI: 10.1103/PhysRevLett.127.100503

With large-scale, error-corrected quantum computers still years away, there has been considerable recent attention in analog quantum simulation (AQS) [1–8]. AQS is a paradigm of quantum computation where a well-controlled artificial system, e.g., a quantum circuit, is constructed to have the same Hamiltonian as a system of interest [9–14]. The dynamics can then be explored by studying the artificial system, i.e., the simulator. Like analog classical computation in the 1960s, AQS is a promising path for unlocking the advantages of quantum computing before large-scale digital quantum computers become feasible.

There is a particular interest in performing quantum simulations of systems that are classically intractable. A broad class of such problems are strongly coupled quantum field theories. These theories include fundamental models such as quantum chromodynamics (QCD), but are also our language to describe a wide array of quantum materials such as high-temperature superconductors. Because of their strong interactions, these theories are not amenable to the standard tools of perturbation theory, making the development of simulation tools critical. While very powerful classical simulation tools exist for some of these problems [15,16], such as lattice QCD, some important problems remain intractable, for instance, due to the infamous sign problem [17]. Since topological models are often affected by the sign problem, they are natural candidates for AQS [18,19].

In this Letter, we present an *in situ* programmable platform for analog quantum simulation. As a demonstration of its potential, we use it for a small-scale simulation of the bosonic Creutz ladder (BCL) [20–22]. The Creutz ladder is a simple quasi-1D lattice model, but nonetheless, exhibits a wide range of interesting behavior including topological and chiral states. It is historically important as one of the first models of chiral lattice fermions [20,23].

The platform we use for AQS is a multimode superconducting parametric cavity. The device has several resonant modes that share a common boundary condition, which is imposed by a superconducting quantum interference device (SQUID). By modulating the shared boundary in time, we induce parametric couplings between modes, including standard "hopping" terms [24–26]. By selecting a set of modulation frequencies, we can create a programmable graph of connections between the modes, which then become the nodes of our lattice arrayed in synthetic dimensions. Because the couplings are created by coherent pump tones, we can control not only the magnitudes of the hopping terms, but also their relative phases. This phase

© 2021 American Physical Society

control allows us to implement models with complex hopping terms, describing classical gauge fields and a variety of topological systems. We further reconstruct the realized Hamiltonian through detailed scattering measurements. We note a recent work that looked at AQS in a parametric cavity, but with a pumping scheme that lacked the addressability and phase control demonstrated here [27].

The Hamiltonian of the infinite Creutz ladder, illustrated in Fig. 1(a), is ($\hbar = 1$)

$$\hat{\mathcal{H}}_C = -\sum_n \bigg[t_d(\hat{b}_n^\dagger \hat{a}_{n+1} + \hat{a}_n^\dagger \hat{b}_{n+1}) + \frac{t_v}{2}(\hat{b}_n^\dagger \hat{a}_n + \hat{a}_{n+1}^\dagger \hat{b}_{n+1}) + t_h e^{i\frac{\phi}{2}}(\hat{a}_{n+1}^\dagger \hat{a}_n + \hat{b}_n^\dagger \hat{b}_{n+1}) \bigg] + \text{H.c.}, \tag{1}$$

where t_d, t_v, t_h are the diagonal, vertical, and horizontal coupling rates and $\phi/2$ is the phase of the horizontal coupling. This Hamiltonian describes the dynamics of a crossed-link fermionic ladder in a magnetic field [20]. There are a number of interesting topological features of the model. As elaborated in our previous work [21], at $\phi = \pi$, the Hamiltonian is time-reversal, particle-hole, and chiral symmetric. Moreover, in the so-called strong coupling limit of $t_v = 0$ and $t_d = t_h = 1$ and with open boundary conditions (finite chain), there are two chiral zero-energy modes localized at the two ends of the ladder. Here, we study the simplest building block one can use to investigate the chiral properties of the Creutz ladder.

We can program the bosonic version of $\hat{\mathcal{H}}_C$ into our parametric cavity with the appropriate choice of pump frequencies. For ease of notation, we will now drop the $\{\hat{a}_n, \hat{b}_n\}$ notation of Eq. (1) and simplify to $\{\hat{a}_n\}$ with the connectivity of the lattice now encoded in a coupling tensor g_{nm}.

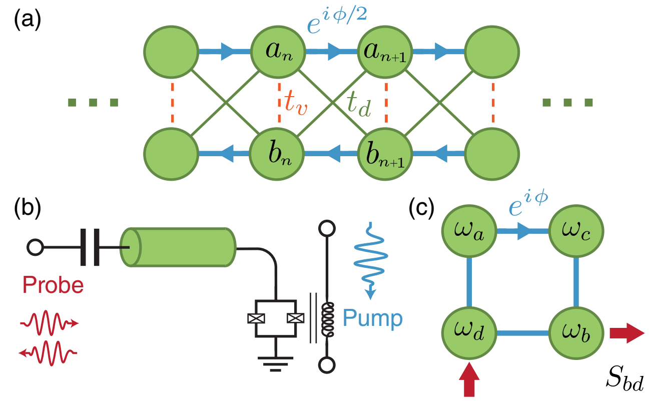

FIG. 1. (a) Schematic representation of the Creutz ladder. The arrows indicate the sign of the hopping phase. (b) Device cartoon. We realize interactions between cavity modes by parametrically pumping the SQUID through a flux line. The system is then probed through the input capacitor by a coherent tone. (c) Synthetic lattice. We program a four-node lattice in synthetic dimensions using four pump tones, which have a well-controlled phase. We measure the scattering matrix of the system by probing near each node frequency and measuring the output at various nodes, which are separated in frequency space.

To probe the system, we must couple it to our measurement line, which we model with the coupling Hamiltonian

$$\hat{\mathcal{H}}_P = i\sum_n \sqrt{\kappa_n^{\text{ext}}}\,(\hat{a}_{i,n} - \hat{a}_{i,n}^\dagger)(\hat{a}_n + \hat{a}_n^\dagger), \tag{2}$$

with $\hat{a}_{i,n}$ describing the annihilation operator of the nth input mode with the external coupling rate κ_n^{ext}. To treat the dynamics of our driven, dissipative system, we use the following Lindblad master equation [28,29]:

$$\dot{\hat{\rho}} = -i[\hat{\mathcal{H}}_C + \hat{\mathcal{H}}_P, \hat{\rho}] + \sum_n \kappa_n \left(\hat{a}_n \hat{\rho} \hat{a}_n^\dagger - \frac{1}{2}\{\hat{a}_n^\dagger \hat{a}_n, \hat{\rho}\} \right),$$

where $\hat{\rho}$ is the reduced density matrix of the plaquette and $\kappa_n = \kappa_n^{\text{ext}} + \kappa_n^{\text{int}}$ is the total photon decay rate including the internal loss rate κ_n^{int} [30].

The Heisenberg-Langevin equations of motion for the mode operators follow directly as:

$$\dot{\hat{a}}_n = i\left(\Delta_n + i\frac{\kappa_n}{2}\right)\hat{a}_n + i\sum_{m\neq n}\frac{g_{nm}}{2}\hat{a}_m + \sqrt{\kappa_n^{\text{ext}}}\hat{a}_{i,n}, \tag{3}$$

where $\Delta_n = \omega_n^s - \omega_n$ with ω_n^s being the probe frequency of the nth mode. Using the input-output formalism, the output modes which we detect are then defined as $\hat{a}_{o,n} = \sqrt{\kappa_n^{\text{ext}}}\hat{a}_n - \hat{a}_{i,n}$. Finally, to find the scattering matrix, we solve for the steady-state solutions of Eq. (3), i.e., assuming $\dot{\hat{a}}_n = 0$, and define $S_{nm} = \langle \hat{a}_{o,n} \rangle / \langle \hat{a}_{i,m} \rangle$. We note that the same scattering equations can be derived from an effective non-Hermitian Hamiltonian [26,31].

The parametric cavity is a quarter wavelength coplanar waveguide resonator terminated by a SQUID at one end and capacitively overcoupled ($Q \approx 7000$) to a 50 Ω transmission line at the other end [24,25,36–38]. The fundamental mode of the cavity is designed to be around 1 GHz, which results in five accessible modes within our measurement bandwidth of 4–12 GHz. We use impedance engineering to make the mode spacing nondegenerate. This enables frequency selective activation of parametric interactions between specific modes, strongly suppressing stray interactions that would, otherwise, arise from accidental degeneracies [24,39]. We can activate a variety of parametric processes by modulating the boundary condition of the cavity using a microwave pump, which is coupled to the SQUID [24–26]. For this work, the hopping terms are activated by pumping at the difference of two mode frequencies.

TABLE I. Extracted device and lattice parameters.

Mode	a	b	c	d
$\omega_n/2\pi$ [GHz]	4.1589	6.0992	7.4726	9.4806
$\kappa_n/2\pi$ [MHz]	1.0113	1.6494	2.9334	4.5804
$\kappa_n^{\text{ext}}/2\pi$ [MHz]	0.43	0.9	2.29	2.89
Coupling	ac	ad	bc	bd
$\omega_{nm}^p/2\pi$ [GHz]	3.3136	5.3223	1.3733	3.382
$\lvert g_{nm}\rvert/2\pi$ [MHz]	2.909	3.707	3.4978	5.650
β_{nm}	0.8446	0.8612	0.7950	1.0278

We program a four-node plaquette by pumping the SQUID with four coherent tones at the appropriate difference frequencies, ω_{nm}^p, as seen in Fig. 1(c). The choice of ω_{nm}^p determines which g_{nm} are nonzero, programming the connection graph of the lattice. As described below, we can associate this small lattice with various parts of a larger Creutz ladder. The mode and pump frequencies are listed in Table I, where we use the specific mode labels $n \in \{a, b, c, d\}$. We generate the pump tones using microwave generators phase locked with 1 GHz references, which provides superior phase coherence.

To characterize the lattice, we use a vector network analyzer (VNA) to probe the system through its input capacitor. To measure the reflection coefficient, $S_{nn}(\Delta_n)$, of node n, we both probe and detect around that node's frequency, ω_n. When the lattice is activated, the single resonance observed at each uncoupled mode frequency is split into a number of resonances. We can interpret this set of resonances as the spectrum of the eigenmodes that exist on the lattice. Each element is centered on the uncoupled mode frequency, and the frequency offset of the coupled eigenmodes can be viewed as the energy of the mode in the common rotating frame of the pumps. We can infer the mode coupling strengths, the g_{nm} of Eq. (3), as a function of pump power from the set of spectra $\{S_{nn}\}$. For the simple case of two coupled modes, the frequency splitting of the eigenmodes directly gives the coupling strength. The situation is more complicated with more than two modes, but the basic intuition is similar.

In setting the coupling strengths for the lattice links, we normalize the coupling strengths to the geometric mean of the mode linewidths κ_m and κ_n, defining $\beta_{nm} = g_{nm}/2\sqrt{\kappa_m \kappa_n}$. Here, we chose the β_{nm} to be roughly equal and in the strong-coupling limit. We use strong coupling, here, to mean that the eigenmodes of the system are resolved in frequency, as seen in Fig. 2. Since different

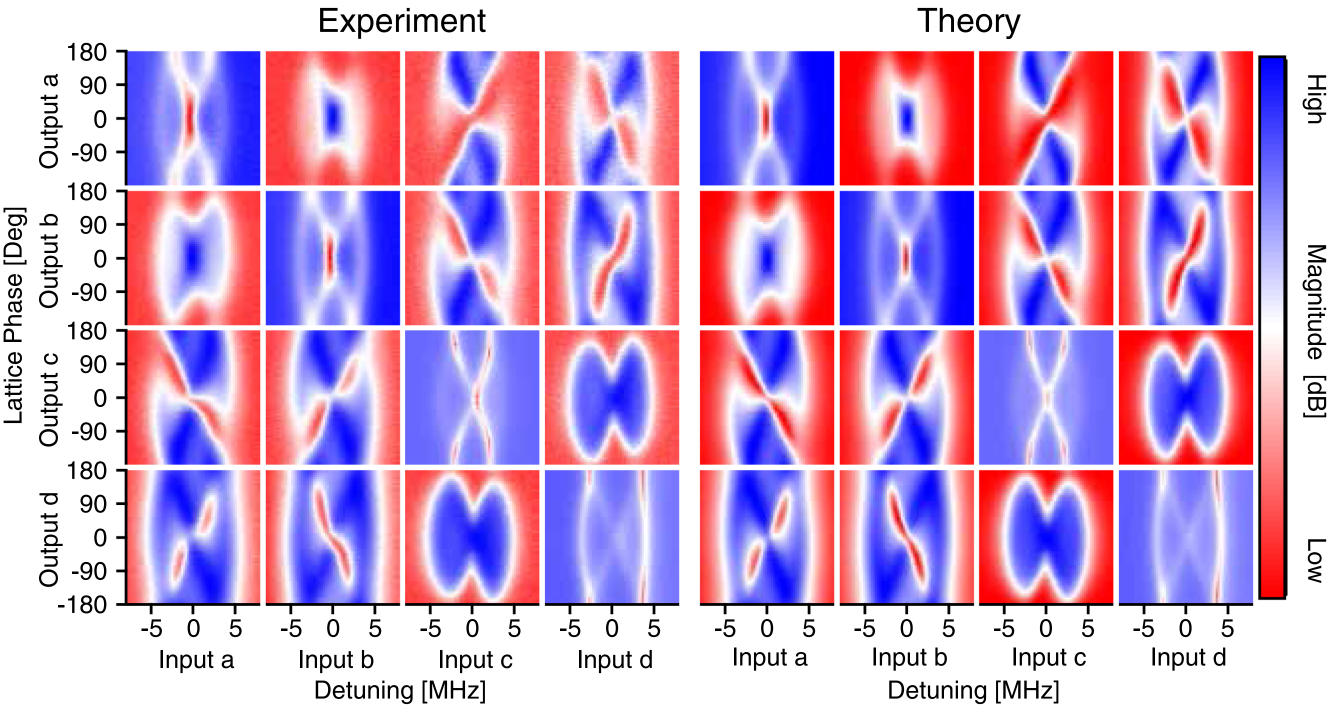

FIG. 2. The scattering matrix. The magnitude of the experimental (left) and theoretical (right) scattering matrices as a function of lattice phase, ϕ, and frequency. The frequency axes give the detunings, Δ_n, from the uncoupled mode frequencies. The diagonal reflection coefficients, $\{S_{nn}\}$, provide the spectrum of the lattice eigenmodes. The off-diagonal elements, $\{S_{mn}\}$, are the magnitude of frequency-converting transport between the nodes. The $\{S_{mn}\}$ allows us to characterize the "spatial" support of each eigenmode over the lattice in the synthetic dimensions (see text). We see, clearly, that the transport is nonreciprocal with $\{S_{mn}\}$ and $\{S_{nm}\}$ often being complements of each other.

lattice nodes exist along synthetic dimensions in frequency space, measuring the off-diagonal scattering coefficients S_{mn}, which characterize transport between nodes, requires a frequency-conversion measurement, where the probe and detection frequencies are offset by ω^p_{nm}. We can distinguish S_{mn} and S_{nm} by swapping the probe and detection frequencies, allowing us to see nonreciprocal features in the transport.

We simulate the effect of applying an external magnetic field to the lattice by making the $\{g_{nm}\}$ complex. The phase of the hopping term represents the phase acquired by an excitation moving along the link in the presence of the magnetic field. For our simple four-node plaquette, only the total phase around the loop matters. As such, we choose, without loss of generality, to sweep the phase, ϕ, of the hopping term between nodes a and c. Formally, moving the phases between links can be seen as a gauge transformation.

Figure 2 shows the measured 4×4 scattering matrix. Each element S_{nm} is measured as a function of ϕ and Δ_n. We clearly see nontrivial behavior as ϕ is varied, with a series of degeneracies arising and disappearing. The off-diagonal elements $\{S_{mn}\}$ show the magnitude of frequency-converting transport from node n to node m. The frequency differences are set by the pump frequencies, ω^p_{nm} (see Table I). These transport measurements allow us to recover spatial information about the support of the eigenmodes over the synthetic lattice. Being in the strong-coupling limit, we can excite a specific eigenmode at a well-defined detuning, Δ_n. As the eigenmodes are "spatially" distributed along the synthetic dimensions, the excitation hops between the nodes and eventually leaks out of the cavity at another node, where it is then detected at the converted frequency.

We performed detailed fitting of the data in Fig. 2. To extract the model parameters, we fit all of the scattering elements simultaneously at several phases [31]. In total, the fit was done to 64 VNA traces simultaneously, so, while the number of parameters is substantial, there is a large amount of data to constrain the fit. Figure 2 also shows the fit scattering matrix. Table I shows the extracted parameters. We find that the quality of the fit is remarkable given the complexity of the data.

We observe a number of interesting features in the scattering matrix. First, we observe clear nonreciprocity in the transport, for instance, noticing that S_{bc} and S_{cb} are effectively complements of each other. The definition of reciprocity is that $S_{ij} = S_{ji}$, which is clearly broken here. We will not emphasize it here, but this can be connected to the fictitious magnetic flux breaking time-reversal symmetry.

We can also identify interesting eigenmodes that we associate with emerging topological features of the Creutz ladder [40]. At $\phi = \pi$, Creutz predicted that the bulk states collapse in a pair of flat bands at equal but opposite energies. A flat band implies that the bulk states are localized, as the group velocity goes to zero. Creutz referred to the associated states as "solitons" and identified the localization as arising from interference between alternate paths on the lattice [see Fig. 3(d)], a phenomenon often referred to as Aharonov-Bohm caging in recent literature. With open boundary conditions, Creutz also predicted the existence of a pair of zero-energy states localized to the ends of the ladder. The connection between the observed eigenmodes and these topological states is discussed in detail in Fig. 3.

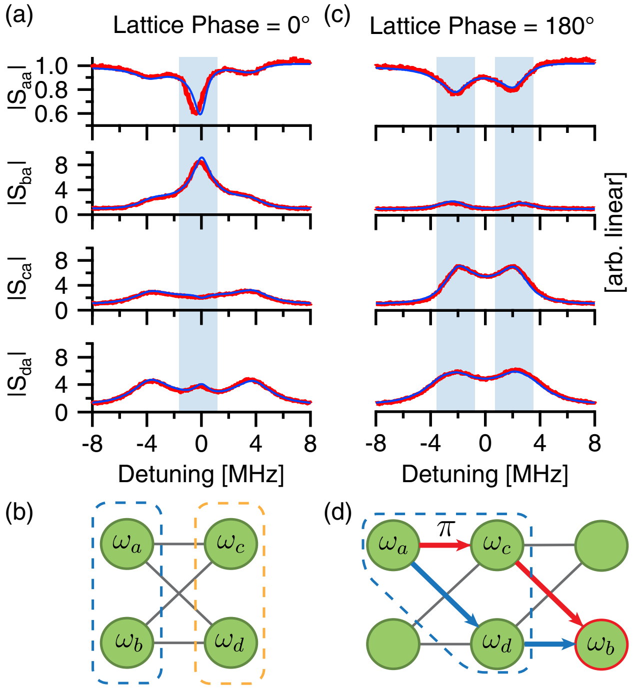

FIG. 3. Topological precursors. (a) $\phi = 0$ line cuts of the measured (red) and theory (blue) scattering parameters in Fig. 2 when probing at node a. The vertical axes are normalized to the background. The measurements indicate the existence of an eigenmode at zero energy with significant support only in nodes a and b, which are not directly connected. We infer this from the relatively high transmission amplitude from a to b. We also observe a second zero mode localized on sites c and d. (b) Twisted plaquette. We expect topological features of the Creutz ladder to appear at $\phi = \pi$ and not $\phi = 0$. However, we note that, if we twist the plaquette as indicated, $\phi = 0$ regardless of the external flux. After twisting, the zero modes now appear at the two ends of the plaquette. These states are reminiscent of the predicted zero-mode end states [20]. (c) $\phi = \pi$ line cuts when probing from node a. The scales of the vertical axes are the same as panel (a). The measurements indicate the existence of two pairs of degenerate eigenmodes, one at positive and one at negative detuning, that have support on all but one of the nodes. One of these four eigenmodes exists on each corner. (d) Caging. We can associate the corner eigenmodes with the soliton states in the Creutz ladder by identifying the lattice as the indicated trapezoidal path. Because of Aharonov-Bohm caging, an excitation at, e.g., node a cannot propagate to node b.

In this Letter, we have introduced a platform for programmable analog quantum simulation of topological lattice models. The platform is hardware efficient, creating the lattice in synthetic dimensions within a single parametric cavity. We have demonstrated the potential of the platform by performing small-scale simulations of a paradigmatic topological model, showing that we can reconstruct the realized Hamiltonian through scattering measurements.

Comparing to competing platforms, such as shaking the optical lattice of a cold-atom system [41] or modulating a harmonic optical cavity [42], we can make the general statement that experimental demonstrations of simulations with complex hopping parameters have generally employed some type of global modulation. While this global approach offers efficiency, it also imposes limitations on uniformity and simulation size, as individual couplings cannot be tuned and, e.g., the global control field will vary across the lattice. Further, the global approach will generally limit the type and complexity of phase patterns, i.e., simulated field configurations, that can be imprinted on the lattice. Last, the accessible connectivity graphs of these approaches is generally both limited and not programmable. Our local approach, with individual amplitude and phase control on every link, circumvents these problems. The obvious trade-off is the relatively large number of control fields required.

We can also consider the scalability of this platform. We can increase the number of nodes in a single cavity in a straightforward manner by increasing the physical length of the cavity, increasing the density of the cavity modes in frequency [27]. Achieving a frequency spacing of 100 MHz is straightforward. This would allow approximately 10 modes per 1 GHz within our 8 GHz of measurement bandwidth. This mode spacing would still easily allow for $g_{nm} \approx 10$–20 MHz without worrying about mode crowding. Although we have not seen any experimental indication of this yet, we do imagine that, eventually, there will be a limit to the number of pump tones we can apply to a single cavity. In that sense, we view this device design as a hardware-efficient building block in a larger system consisting of many of these cavities parametrically coupled to each other [43]. Each individual cavity would then be a sublattice stitched together into a larger lattice made of several cavities. Devices made from hundreds of coupled cavities on a single chip have been demonstrated [44]. Further discussion of scalability can be found in the Supplemental Material [31].

While we have emphasized, as a demonstration, the simulation of a quasi-1D lattice, the platform is easily extensible to two dimensions (or higher). Essentially, the connection graph of the simulated lattice is arbitrary and the dimensionality of the simulation is set by the number of nearest-neighbor connections of each node. As an example of possible physics to explore, Ref. [45] proposed a pattern of hopping phases that produces an effective (magnetic) gauge field for photons in a 2D photonic lattice like ours.

The node-to-node coupling demonstrated here can be extended in a number of promising and interesting ways. Here, we only activated the simplest type of coupling (hopping). Another well-characterized parametric process is two-photon parametric down-conversion, which would be activated by pumping at the sum of two mode frequencies, adding Hamiltonian terms of the form $\hat{a}_i^\dagger \hat{a}_j^\dagger$. First, this is interesting as it is a source of nonclassical states, including squeezed and entangled states. We have also shown, previously, that combining hopping and down-conversion can create scalable, multimode entangled states [24]. Next, down-conversion unlocks a number of interesting simulation effects. For instance, the two-photon process can mimic a pairing potential [46], as in superconductivity. Further, combining down-conversion and hopping terms leads directly to chiral and topological features, as in the bosonic Kitaev-Majorona chain [46]. Finally, down-conversion provides access to coherent non-Hermitian Hamiltonians, in contrast to the loss-induced non-Hermiticity widely studied in the literature [47,48].

Both hopping and two-photon down-conversion are examples of Gaussian processes. However, our group and others have recently demonstrated a variety of higher-order non-Gaussian processes [49,50], including three-photon spontaneous parametric down-conversion [25]. Beyond broadening the type of photonic states that we can introduce into the system, including non-Gaussian entangled states [51], these multiphoton processes can create many-body interactions, e.g., of the form $\hat{a}_i \hat{a}_j^\dagger \hat{a}_k^\dagger$, that are one key route to realizing simulations of dynamical gauge fields [19,52]. Further, it has recently been shown that these processes can induce a strong, tunable nonlinearity when used to couple a pair of harmonic modes [49]. This stimulated nonlinearity is significant at the single-photon level, providing another way that we can add effective photon-photon interactions to the system. All of the various effects mentioned here have been demonstrated experimentally in parametric cavities and their incorporation into simulations is the subject of ongoing work.

The authors wish to thank B. Plourde, J. J. Nelson, and M. Hutchings at Syracuse University for invaluable help in junction fabrication. H. A. acknowledges financial support from the Eliteprogram Grant of Baden-Württemberg Stiftung and the Purdue University Start-up Grant. E. R. thanks the QuantERA Project QTFLAG, and support of the Basque Government Grant No. IT986-16. E. S. acknowledges support from the projects QMiCS (Grant No. 820505) and OpenSuperQ (Grant No. 820363) of the EU Flagship on Quantum Technologies, Spanish MINECO/FEDER Grant No. FIS2015-69983-P, Basque Government Grant No. IT986-16, EU FET Open Grants Quromorphic, EPIQUS, and Shanghai STCSM (Grant No. 2019SHZDZX01-ZX04). C. M. W., J. S. C. H., J. B.,

C. W. S. C., A. M. V., and I. N. acknowledge the Canada First Research Excellence Fund (CFREF), NSERC of Canada, the Canadian Foundation for Innovation, the Ontario Ministry of Research and Innovation, and Industry Canada for financial support.

J. S. C. H. and J. H. B. contributed equally to this Letter.

---

[*] chris.wilson@uwaterloo.ca

[1] A. Sørensen and K. Mølmer, Phys. Rev. Lett. **82**, 1971 (1999).

[2] J. Argello-Luengo, A. Gonzlez-Tudela, T. Shi, P. Zoller, and J. I. Cirac, Nature (London) **574**, 215 (2019).

[3] A. Blais, R.-S. Huang, A. Wallraff, S. M. Girvin, and R. J. Schoelkopf, Phys. Rev. A **69**, 062320 (2004).

[4] A. Blais, S. M. Girvin, and W. D. Oliver, Nat. Phys. **16**, 247 (2020).

[5] P. J. Lee, K.-A. Brickman, L. Deslauriers, P. C. Haljan, L.-M. Duan, and C. Monroe, J. Opt. B **7**, S371 (2005).

[6] B. P. Lanyon, J. D. Whitfield, G. G. Gillett, M. E. Goggin, M. P. Almeida, I. Kassal, J. D. Biamonte, M. Mohseni, B. J. Powell, M. Barbieri, A. Aspuru-Guzik, and A. G. White, Nat. Chem. **2**, 106 (2010).

[7] A. Aspuru-Guzik, A. D. Dutoi, P. J. Love, and M. Head-Gordon, Science **309**, 1704 (2005).

[8] F. Mei, G. Chen, L. Tian, S.-L. Zhu, and S. Jia, Phys. Rev. A **98**, 012331 (2018).

[9] R. Islam, R. Ma, P. M. Preiss, M. Eric Tai, A. Lukin, M. Rispoli, and M. Greiner, Nature (London) **528**, 77 (2015).

[10] H. Bernien, S. Schwartz, A. Keesling, H. Levine, A. Omran, H. Pichler, S. Choi, A. S. Zibrov, M. Endres, M. Greiner, V. Vuleti, and M. D. Lukin, Nature (London) **551**, 579 (2017).

[11] J. T. Barreiro, M. Mller, P. Schindler, D. Nigg, T. Monz, M. Chwalla, M. Hennrich, C. F. Roos, P. Zoller, and R. Blatt, Nature (London) **470**, 486 (2011).

[12] K. R. Brown, J. Kim, and C. Monroe, npj Quantum Inf. **2**, 16034 (2016).

[13] J. Braumller, M. Marthaler, A. Schneider, A. Stehli, H. Rotzinger, M. Weides, and A. V. Ustinov, Nat. Commun. **8**, 779 (2017).

[14] N. K. Langford, R. Sagastizabal, M. Kounalakis, C. Dickel, A. Bruno, F. Luthi, D. J. Thoen, A. Endo, and L. DiCarlo, Nat. Commun. **8**, 1715 (2017).

[15] S.-J. Ran, E. Tirrito, C. Peng, X. Chen, L. Tagliacozzo, G. Su, and M. Lewenstein, *Tensor Network Contractions: Methods and Applications to Quantum Many-Body Systems*, Lecture Notes in Physics (Springer International Publishing, New York, 2020).

[16] E. Zohar and J. I. Cirac, Phys. Rev. D **97**, 034510 (2018).

[17] T. Dornheim, Phys. Rev. E **100**, 023307 (2019).

[18] T. Sulejmanpasic and C. Gattringer, Nucl. Phys. **B943**, 114616 (2019).

[19] M. C. Bañuls, R. Blatt, J. Catani, A. Celi, J. I. Cirac, M. Dalmonte, L. Fallani, K. Jansen, M. Lewenstein, S. Montangero, C. A. Muschik, B. Reznik, E. Rico, L. Tagliacozzo, K. Van Acoleyen, F. Verstraete, U.-J. Wiese, M. Wingate, J. Zakrzewski, and P. Zoller, Eur. Phys. J. D **74**, 165 (2020).

[20] M. Creutz, Phys. Rev. Lett. **83**, 2636 (1999).

[21] H. Alaeian, Chung Wai Sandbo Chang, M. V. Moghaddam, C. M. Wilson, E. Solano, and E. Rico, Phys. Rev. A **99**, 053834 (2019).

[22] J. Zurita, C. E. Creffield, and G. Platero, Adv. Quantum Technol. **3**, 1900105 (2020).

[23] D. B. Kaplan, arXiv:0912.2560.

[24] C. W. Sandbo Chang, M. Simoen, J. Aumentado, C. Sabín, P. Forn-Díaz, A. M. Vadiraj, F. Quijandría, G. Johansson, I. Fuentes, and C. M. Wilson, Phys. Rev. Applied **10**, 044019 (2018).

[25] C. W. Sandbo Chang, C. Sabín, P. Forn-Díaz, F. Quijandría, A. M. Vadiraj, I. Nsanzineza, G. Johansson, and C. M. Wilson, Phys. Rev. X **10**, 011011 (2020).

[26] F. Lecocq, L. Ranzani, G. A. Peterson, K. Cicak, R. W. Simmonds, J. D. Teufel, and J. Aumentado, Phys. Rev. Applied **7**, 024028 (2017).

[27] N. R. A. Lee, M. Pechal, E. A. Wollack, P. Arrangoiz-Arriola, Z. Wang, and A. H. Safavi-Naeni, Phys. Rev. A **101**, 053807 (2020).

[28] G. Lindblad, Commun. Math. Phys. **48**, 119 (1976).

[29] C. Gardiner and P. Zoller, *Quantum Noise: A Handbook of Markovian and Non-Markovian Quantum Stochastic Methods with Applications to Quantum Optics*, 3rd ed., Springer Series in Synergetics (Springer-Verlag, Berlin, 2004).

[30] Here, we are mainly interested in the dynamics of cavity modes so the transmission-line bath can be integrated out in the typical Lindblad form. The material loss inside the cavity leads to additional decay which we could either be included as a non-Hermitian term κ_n^{int} or directly incorporated in the Lindblad form. If the latter, their noise input contribution and corresponding input or output formalism must be treated differently. While the coupling to the transmission line leads to input noise terms, the internal loss noise contribution should be governed by the fluctuation-dissipation theorem at equilibrium temperature.

[31] See Supplemental Material at http://link.aps.org/supplemental/10.1103/PhysRevLett.127.100503 for details of fitting and further discussion of basic features of the BCL, which includes Refs. [32–35].

[32] A. Dunsworth *et al.*, Appl. Phys. Lett. **111**, 022601 (2017).

[33] R. Resta and D. Vanderbilt, in *Physics of Ferroelectrics: A Modern Perspective*, Topics in Applied Physics (Springer, Berlin, Heidelberg, 2007), pp. 31–68.

[34] C. R. H. McRae, H. Wang, J. Gao, M. Vissers, T. Brecht, A. Dunsworth, D. Pappas, and J. Mutus, arXiv:2006.04718.

[35] M. S. Khalil, M. J. Stoutimore, F. C. Wellstood, and K. D. Osborn, J. Appl. Phys. **111**, 054510 (2012).

[36] M. Sandberg, C. M. Wilson, F. Persson, T. Bauch, G. Johansson, V. Shumeiko, T. Duty, and P. Delsing, Appl. Phys. Lett. **92**, 203501 (2008).

[37] C. M. Wilson, T. Duty, M. Sandberg, F. Persson, V. Shumeiko, and P. Delsing, Phys. Rev. Lett. **105**, 233907 (2010).

[38] M. Simoen, C. W. S. Chang, P. Krantz, J. Bylander, W. Wustmann, V. Shumeiko, P. Delsing, and C. M. Wilson, J. Appl. Phys. **118**, 154501 (2015).

[39] E. Zakka-Bajjani, F. Nguyen, M. Lee, L. R. Vale, R. W. Simmonds, and J. Aumentado, Nat. Phys. **7**, 599 (2011).

[40] A common way to identify topological states is through an invariant such as the Chern number. While the value of these

invariants can be inferred from the fully reconstructed Hamiltonian we have extracted, our theoretical investigations suggest that these invariants do not carry meaningful information on a single plaquette.

[41] J. H. Kang, J. H. Han, and Y. Shin, New J. Phys. **22**, 013023 (2020).

[42] A. Dutt, Q. Lin, L. Yuan, M. Minkov, M. Xiao, and S. Fan, Science **367**, 59 (2020).

[43] B. Peropadre, D. Zueco, F. Wulschner, F. Deppe, A. Marx, R. Gross, and J. J. García-Ripoll, Phys. Rev. B **87**, 134504 (2013).

[44] A. A. Houck, H. E. Treci, and J. Koch, Nat. Phys. **8**, 292 (2012).

[45] K. Fang, Z. Yu, and S. Fan, Nat. Photonics **6**, 782 (2012).

[46] A. McDonald, T. Pereg-Barnea, and A. A. Clerk, Phys. Rev. X **8**, 041031 (2018).

[47] T. Ozawa, H. M. Price, A. Amo, N. Goldman, M. Hafezi, L. Lu, M. C. Rechtsman, D. Schuster, J. Simon, O. Zilberberg, and I. Carusotto, Rev. Mod. Phys. **91**, 015006 (2019).

[48] Z. Gong, Y. Ashida, K. Kawabata, K. Takasan, S. Higashikawa, and M. Ueda, Phys. Rev. X **8**, 031079 (2018).

[49] A. Vrajitoarea, Z. Huang, P. Groszkowski, J. Koch, and A. A. Houck, Nat. Phys. **16**, 211 (2020).

[50] R. Lescanne, M. Villiers, T. Peronnin, A. Sarlette, M. Delbecq, B. Huard, T. Kontos, M. Mirrahimi, and Z. Leghtas, Nat. Phys. **16**, 509 (2020).

[51] A. Agustí, C. W. Sandbo Chang, F. Quijandría, G. Johansson, C. M. Wilson, and C. Sabín, Phys. Rev. Lett. **125**, 020502 (2020).

[52] J. Jünemann, A. Piga, S. J. Ran, M. Lewenstein, M. Rizzi, and A. Bermudez, Phys. Rev. X **7**, 031057 (2017).